Schweizerischer Erdbebendienst
Service Sismologique Suisse
Servizio Sismico Svizzero
Swiss Seismological Service

ETH zürich

SITE CHARACTERIZATION REPORT

SMELS: Mels (SG), Schulhaus Feldacker

Agostiny Marrios Lontsi, Manuel Hobiger, Donat Fäh

Last Modification: 28th May, 2020

Schweizerischer Erdbebendienst (SED)
Service Sismologique Suisse
Servizio Sismico Svizzero
Servizi da Terratrembels Svizzer

ETH Zürich
Sonneggstrasse 5
8092 Zürich
Schweiz
agostiny.lontsi@sed.ethz.ch

Contents

Summary

A passive seismic survey was conducted at the strong-motion station SMELS at Mels (SG) to characterize the underlying subsurface. The geophysical site characterization aims at using ambient seismic vibration recordings to infer the shear-wave velocity profile around the installed seismological station.

The H/V and ellipticity measurements show that the fundamental frequency of the site is about 1.15 Hz.

The array methods used include high-resolution frequency-wavenumber, wavefield decomposition, interferometric-MASW, and spatial autocorrelation. They provide clear phase velocity dispersion curves for Rayleigh and Love waves. Two Rayleigh wave branches are observed and interpreted as fundamental and first higher modes. Two Love wave branches are also observed and interpreted as fundamental mode and first higher mode.

Two combined inversions are performed, one inverting ellipticity information and dispersion curves and the second combining the full H/V and dispersion curves. The resulting best velocity profiles indicate three major discontinuities at around 18, 60, and 260 m depth. The average V_{S30} from the best shear wave velocity profiles of the site is 404.9 $\pm$ 9.5 m/s. This V_{S30} value corresponds to ground type B in EC8 (European standard) and to ground type C in SIA261 (Swiss standard).

1 Introduction

As part of the second phase of the Swiss Strong Motion Network renewal project, a strong motion station was built close to the Schulhaus Feldacker in Mels. The station went operational on July 17^{th}, 2018. At this site, a passive seismic survey was performed to record the propagating ambient noise wavefield. We use surface wave methods to analyze the contribution of Rayleigh and Love waves to the recorded noise wavefields. The estimated phase velocity dispersion and the ellipticity information are combined in an inversion process to infer the underlying subsurface structure and the corresponding 1D shear wave velocity profile. In a second inversion, we test the full H/V inversion code constrained with phase velocity dispersion curves.

2 Site and geological setting

Figure 1a) shows the location of Mels in Switzerland. Zooms are shown in Figures 1b) and 1c). The zoom in Figure 1b) shows the location of the strong motion station SMELS overlayed on the background topography map. The zoom in Figure 1c) shows the subsurface geology around SMELS. Most of the stations sit on creek deposits. The station MELS44 clearly sits on alluvial deposits.

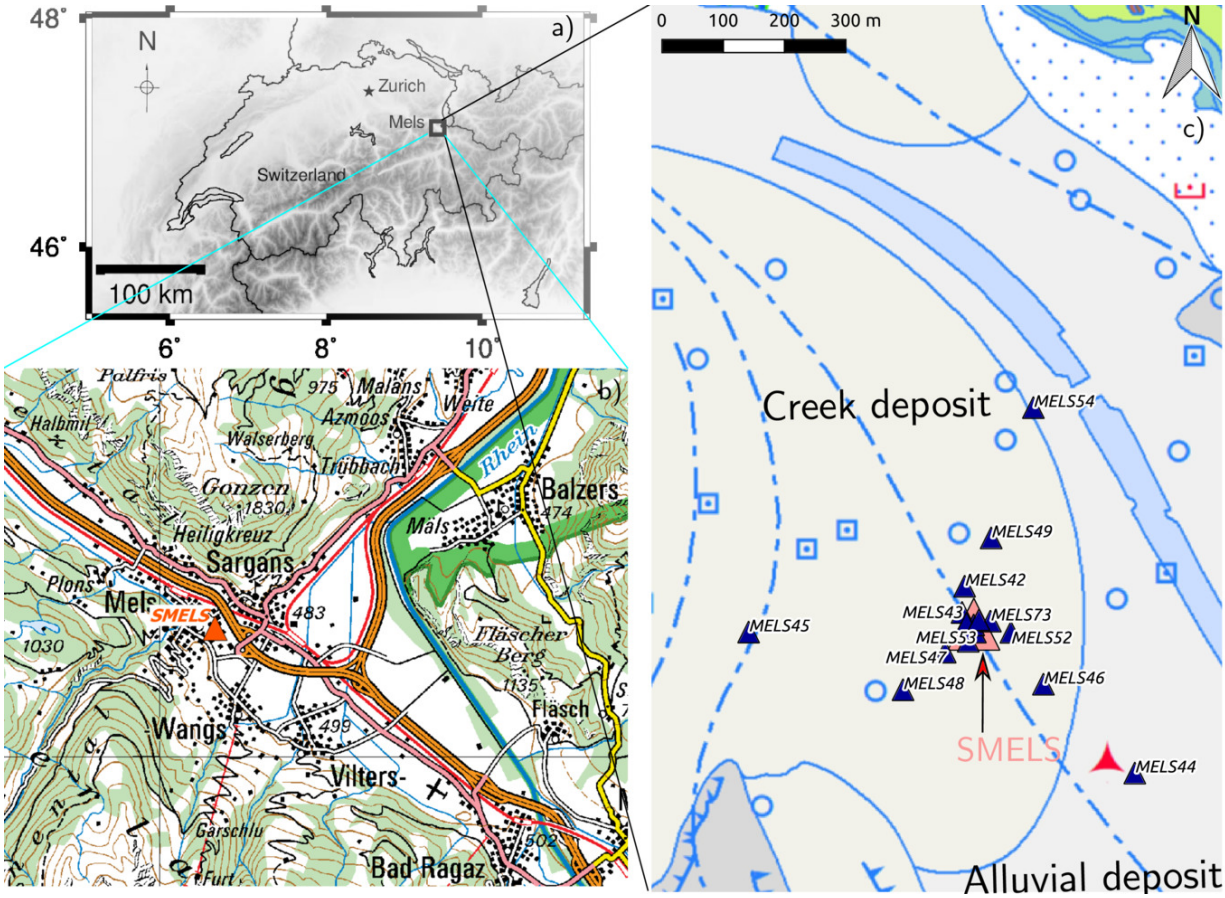

Figure 1: a) Location of the test site at Mels (SG), Switzerland. b) A zoom of the test site where the strong motion station SMELS is located. c) Subsurface geology at the measurement site.

3 Overview of the site characterization measurement

In order to characterize the local underground structure around station SMELS, a passive seismic array measurements was carried out on October 8^{th}, 2019. Figure 2 shows an aerial image of the survey site, indicating the permanent station SMELS (triangle at the center with light red color) and the temporary array deployment (with blue triangles) for ambient noise measurements. The array consisted of 16 stations. It was planned to consist of five rings of three stations each around a central station. The minimum and maximum inter-station distances of the final array layout were 11.93 and 671.27 m, respectively. The seismic stations consisted of Lennartz 3C 5 s sensors connected to Centaur digitizers. A total of 12 digitizers were used. Twelve sensors were connected to the A channels of the digitizers and another four sensors were connected to the B channels. The sampling rate was 200 Hz.
In addition to the array deployment, two rotational sensors were deployed next to the strong motion station SMELS (see Figure 3).

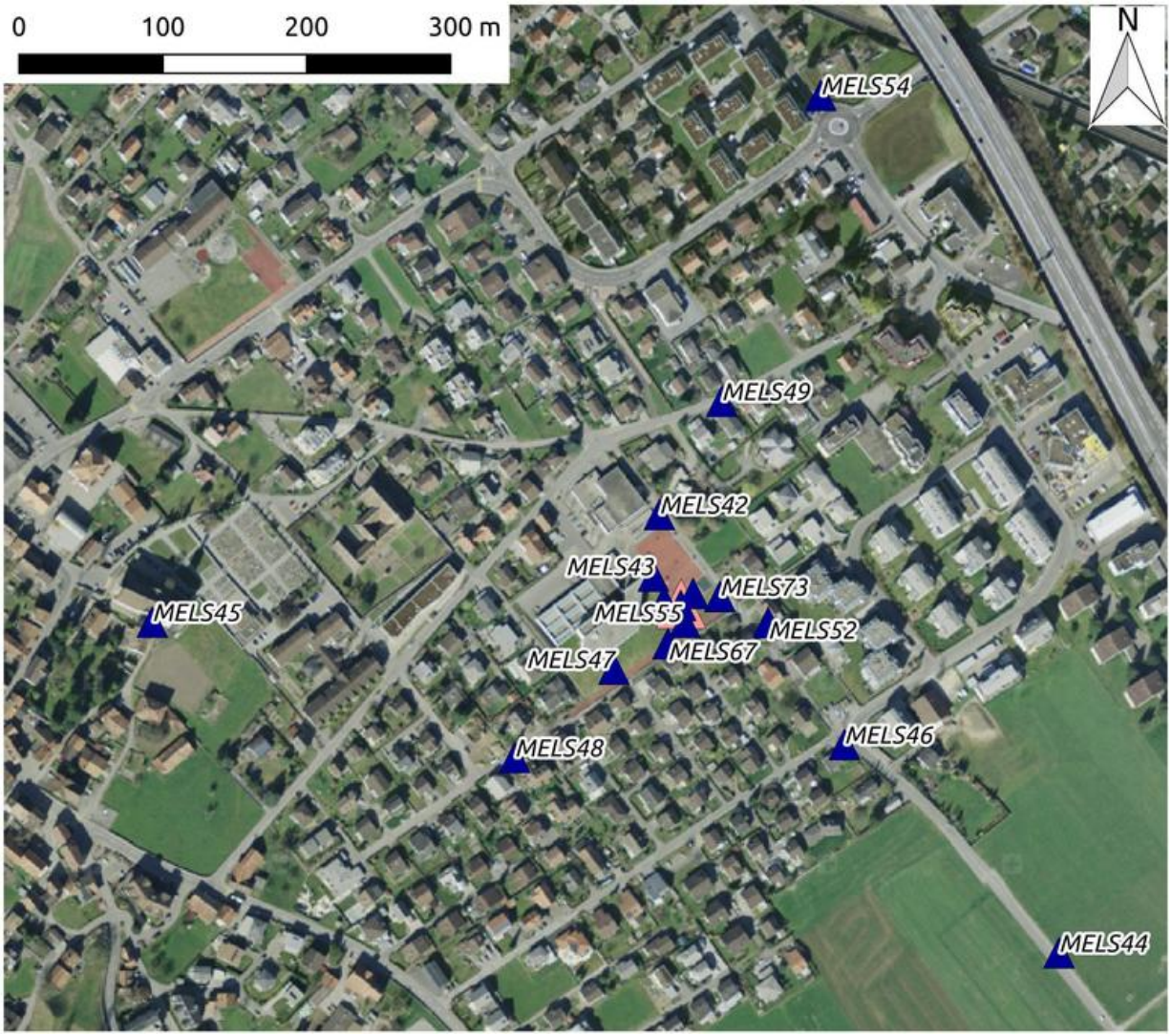

Figure 2: Background topography, strong motion station location and array configuration. ©2020 swisstopo (JD100042).

Figure 3: Rotational and translational (MELS55) sensors around the permanent strong motion station (SMELS).

The array continously recorded ambient vibrations for 2h15min between 11:55 and 14:10 (UTC).
The station locations have been measured by a differential GPS system (Leica Viva GS10) which was set up to measure with a precision better than 5 cm. This precision was achieved at most stations except at station MELS45 where no differential GPS connection could be established and the precision was worse than 2 m. The coordinates of this station were obtained from map.geo.admin.ch.

4 Single-station analysis

4.1 Misorientation correction using the rotational sensor

The rotational sensor was installed as part of a test, but the data are not used here. Nevertheless, this sensor indicates the north direction very precisely and we used it to correct the misorientations of the array sensors. The iXblue sensor was oriented in line with station SMELS55, the central station of the array. The rotation sensor indicated a misorientation of 11.56° (towards east). We corrected SMELS55 by this value and determined the misorientations of the other stations by cross-correlating them with station SMELS55 in a frequency range from 0.3 to 1.0 Hz. The misorientations range

from -4.11° to 10.25°.

4.2 Microtremor H/V and ellipticity estimation

The microtremor H/V spectral ratio and the ellipticity are obtained using 6 different techniques:

- geopsyhv: full microtremor H/V estimation (www.geopsy.org);
- RayDec, optimized for Rayleigh wave ellipticity estimation (Hobiger et al., 2009);
- FTAN, optimized for Rayleigh wave ellipticity estimation (Fäh et al., 2009);
- CLASS, optimized for Rayleigh wave ellipticity estimation, (Fäh et al., 2001);
- VPTFA, optimized for Rayleigh wave ellipticity estimation (Poggi & Fäh, 2010);
- MTSPEC, optimized for Rayleigh wave ellipticity estimation (Burjánek et al., 2010).

The H/V results for each station using the 6 techniques are shown in Figure 4 for comparison. In general, the H/V spectral ratio shows a very stable peak at about 1.15 Hz. For each station, two peak frequencies are picked (Figure 5).
Most stations show one major frequency peak at frequencies between 0.95 Hz (MELS75) and 1.16 Hz (MELS49), which suggests that the subsurface structure has one main strong impedance contrast at similar depths at all stations. Station MELS54 shows an H/V curve that differs from all other stations. This station was the northernmost one of the array and located close to the highway, that also has a bridge close by. Either the structure there differs a lot from the rest of the array or the station was perturbed by the close noise sources on the highway or the eigenvibrations of the bridge.

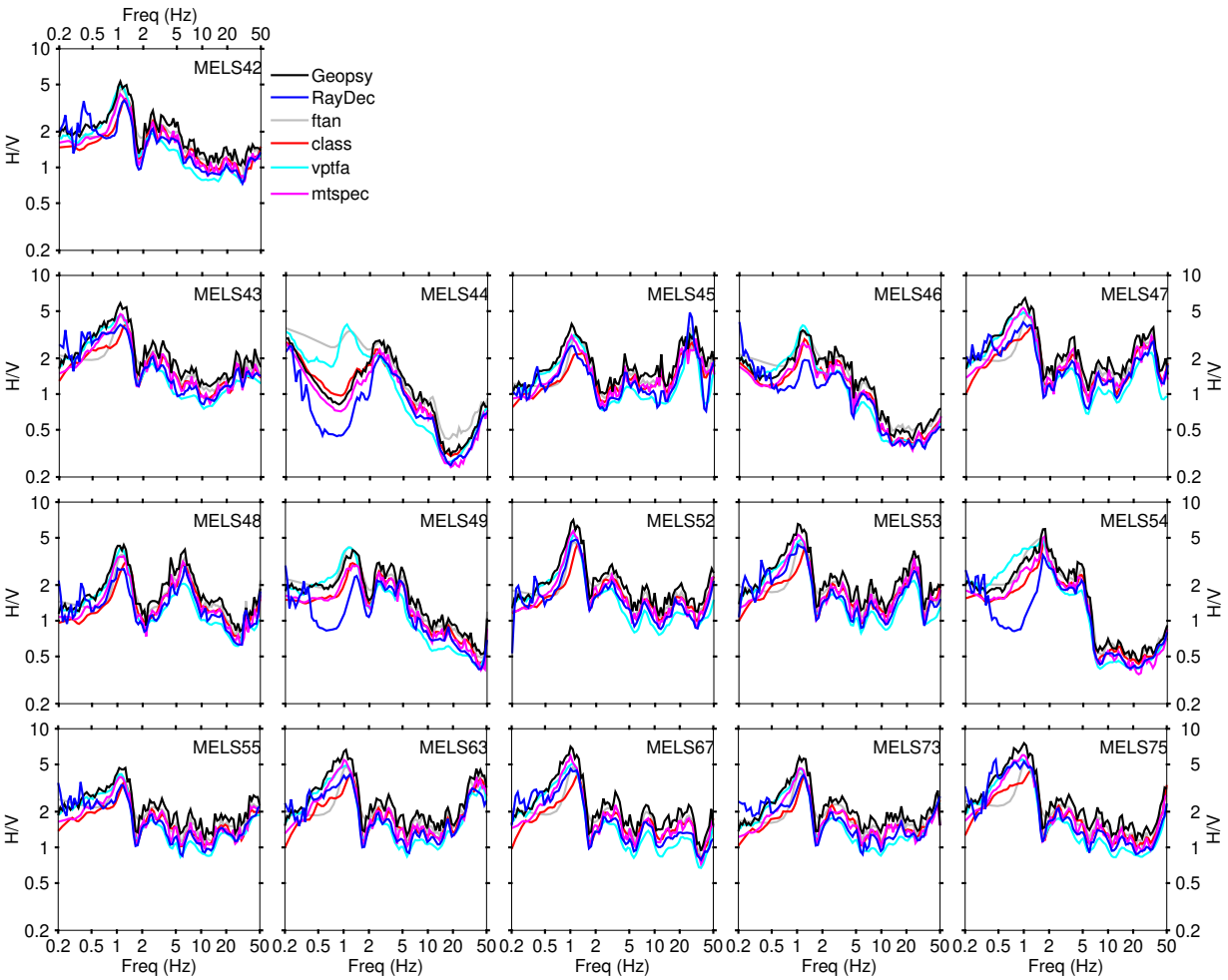

Figure 4: Ellipticity and H/V spectral ratio estimation using different techniques.

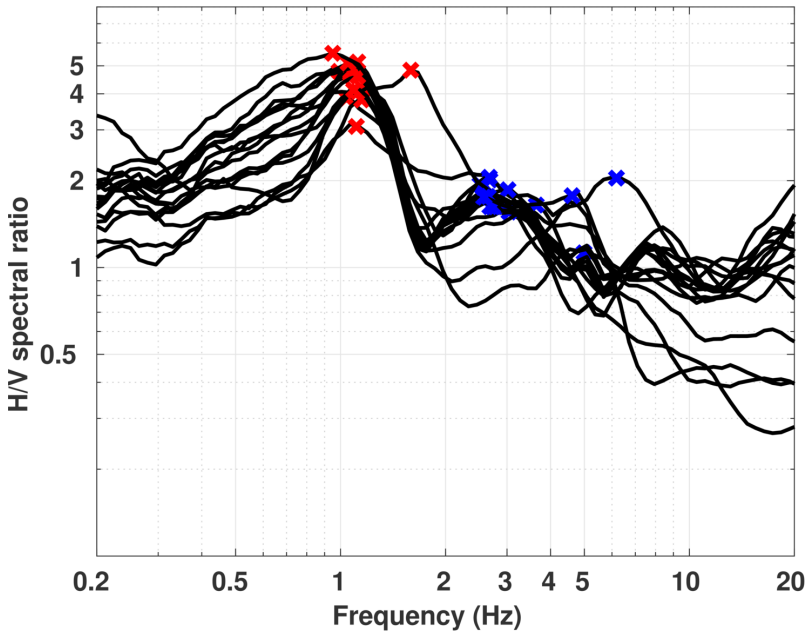

Figure 5: Overview of the H/V curves of the different stations, obtained using the ellipticity technique by Poggi & Fäh (2010); see also *vptfa* on Figure 4. The red and blue markers indicate the frequencies of the first and second maxima in the H/V spectral ratio curves.

4.3 Polarization analysis

Following Burjánek et al. (2010, 2012), the polarization analysis is performed to assess potential 2D effects. The results are shown in Figure 6 for station MELS55, the central station of the array.

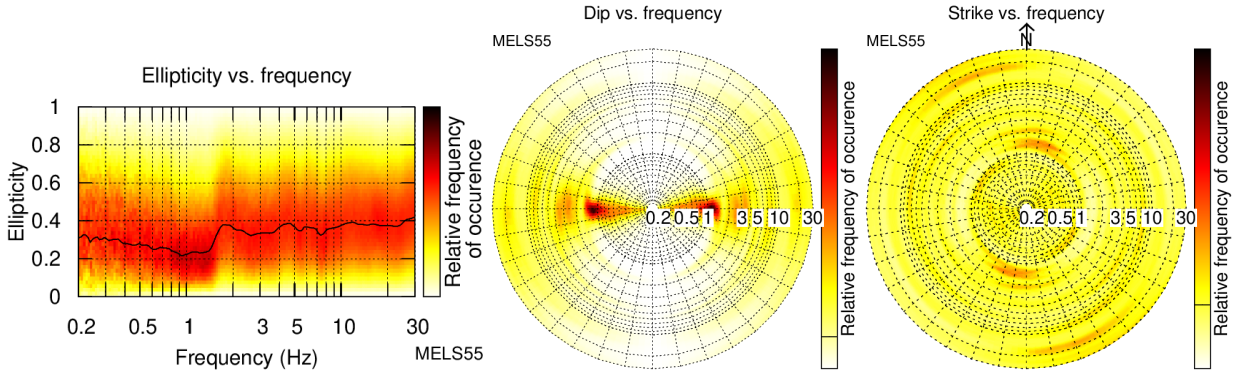

Figure 6: Polarization analysis for the station SMELS located next to the permanent station.

We observe no preferential strike direction and no indication for 2-dimensional polarization effects.

5 Array analysis

The phase velocities for Rayleigh and Love waves are estimated for the full array of 16 stations using three different array methods:

- Spatial autocorrelation (SPAC, Aki 1957; Bettig et al. 2001).
- High resolution frequency-wavenumber (HRFK, Poggi & Fäh 2010);
- Interferometric Multichannel Analysis of Surface Waves (IMASW, Lontsi et al. 2016)
- Wavefield decomposition (WaveDec, Maranò et al. 2012);

The results of the dispersion curve analysis are presented in Figure 7 for SPAC, in Figure 8 for HRFK, in Figure 9 for IMASW, and in Figure 10 for WaveDec.

5.1 SPAC

The SPAC (Aki, 1957) curves of the vertical components have been calculated using the M-SPAC (Bettig et al., 2001) technique implemented in geopsy. Rings with different radius ranges had been defined and for all station pairs with distance inside this radius range, the cross-correlation was calculated over a wide frequency range. These cross-correlation curves are averaged for all station pairs of the respective ring and give the SPAC curves.
The SPAC rings are shown in Figure 7(top). The phase velocity is obtained through a non-linear inversion of the estimated autocorrelation coefficients. This was made with the function spac2disp of the geopsy package. Using SPAC, we can retrieve a Rayleigh wave dispersion curve between 1.56 and 8.3 Hz.

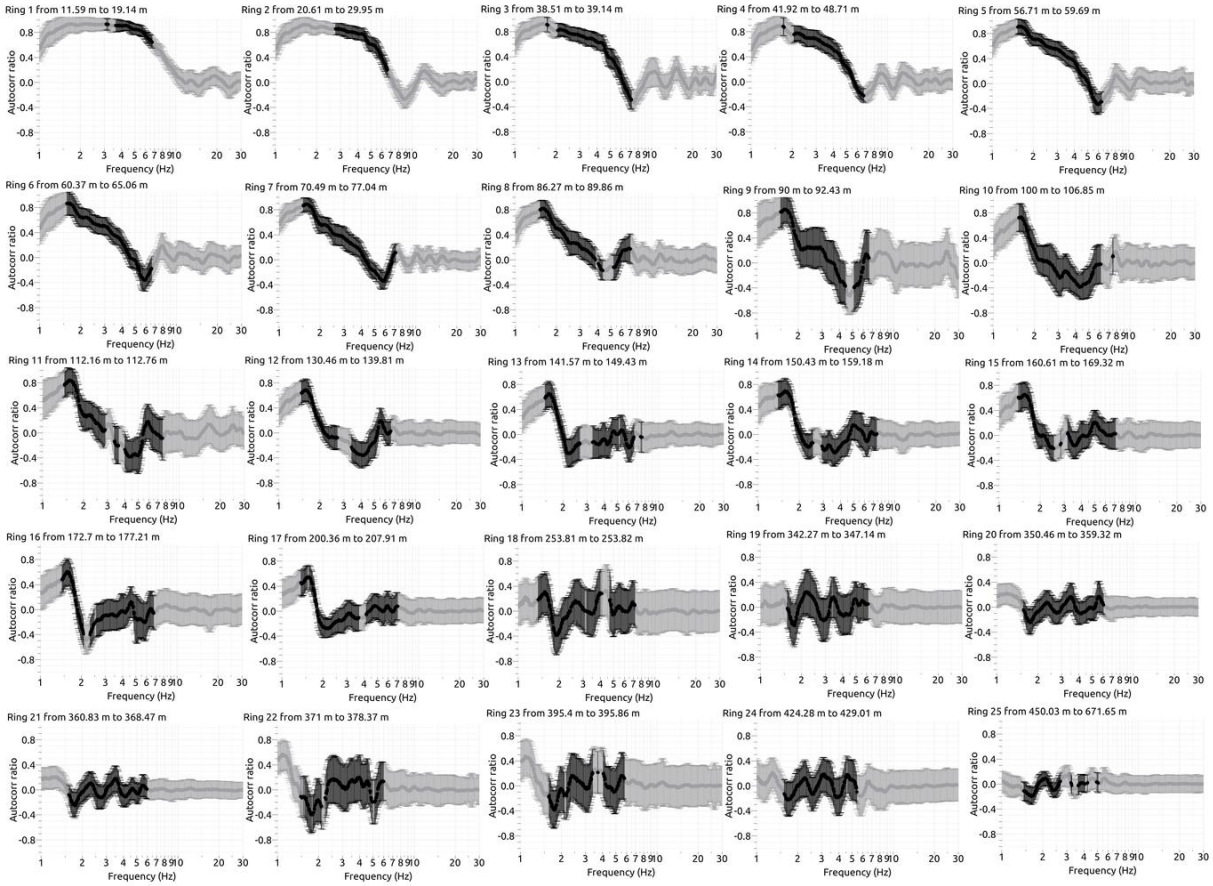

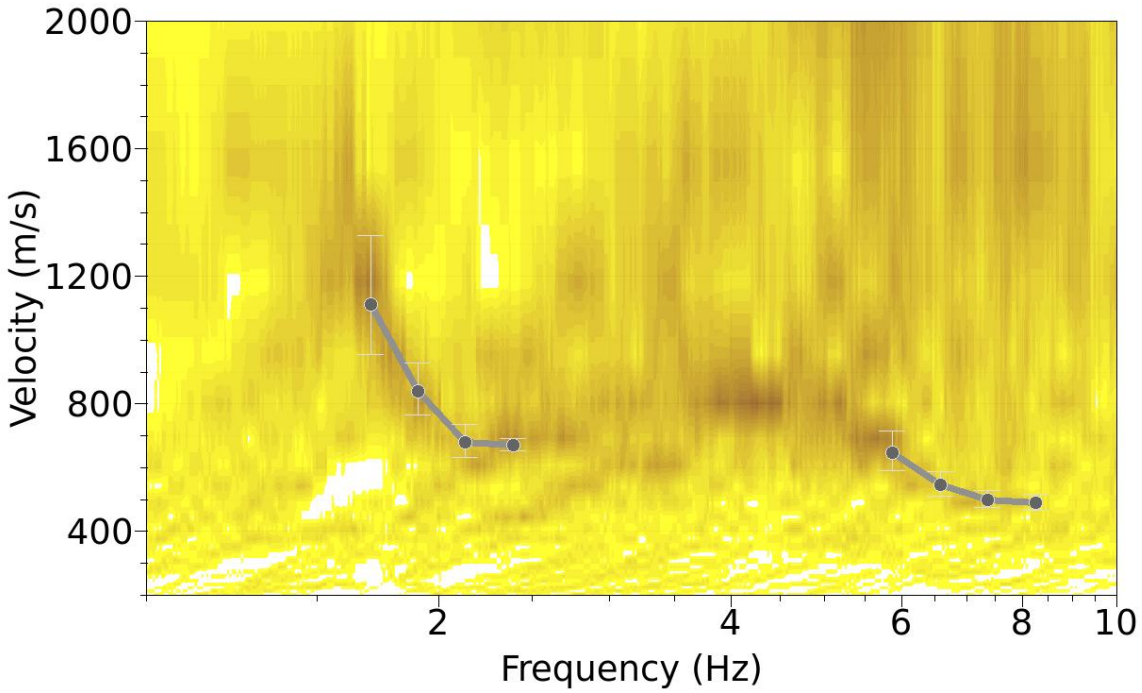

Figure 7: SPAC results. The picked phase velocity dispersion branches are represented by the grey curves.

5.2 HRFK

We picked within the resolution limits (represented by the dashed and dotted black lines in Figure 8) the transverse (Love waves) and vertical (Rayleigh waves) phase velocity dispersion curves (represented by the green curves). The integration of the results allow us to obtain phase velocity dispersion curves for Rayleigh and Love waves in a very large frequency band that ranges from 1.75 to 16.71 Hz. On the vertical component, the attribution of the modes is difficult and we picked several branches. We will try to attribute them later. On the radial component, the results were much more scattered than on the vertical component and no dispersion curves were picked.

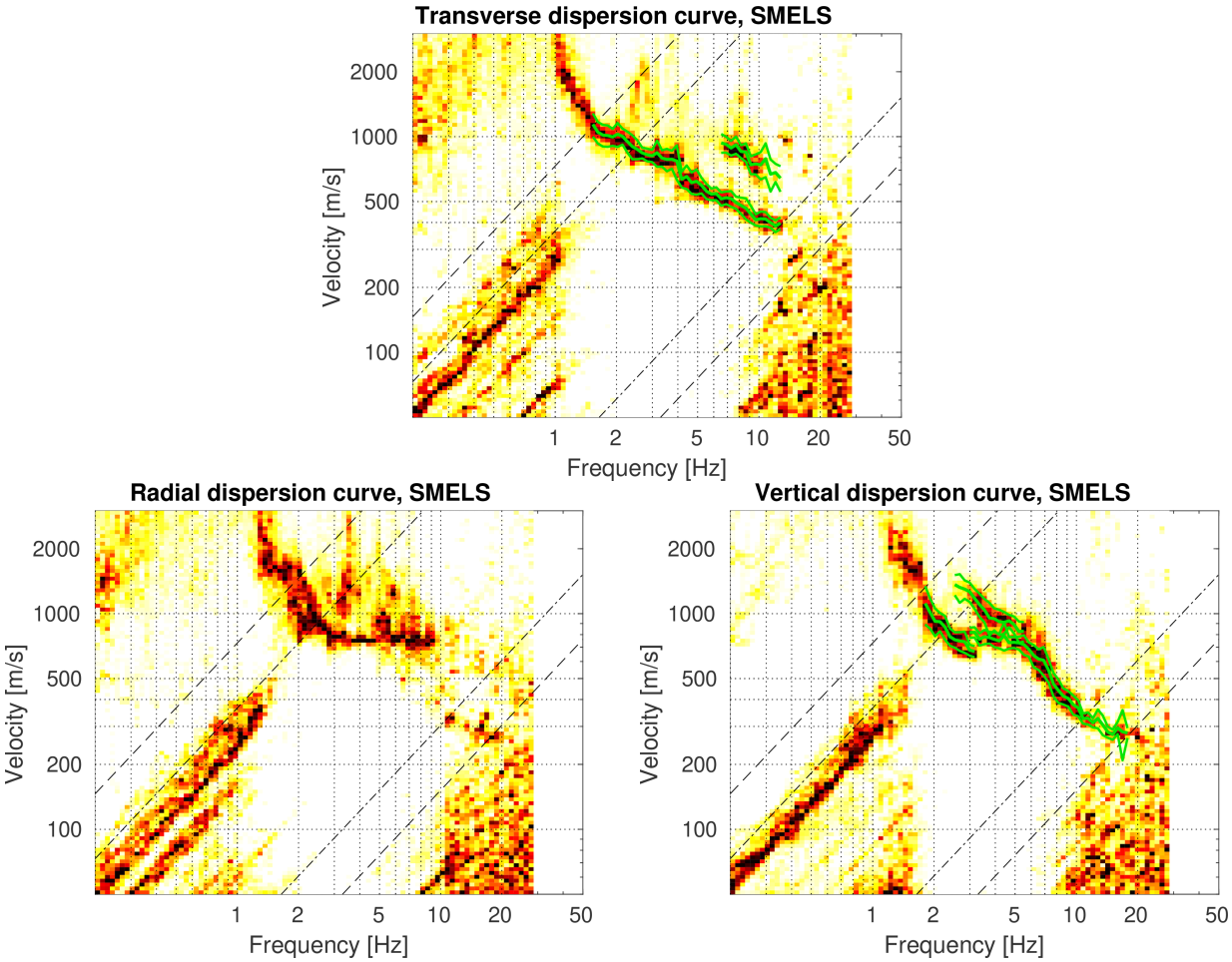

Figure 8: HRFK results. The phase velocity dispersion curves on the three components are shown. The phase velocity dispersion branches are picked within the array resolution limits on the transverse component for Love waves and on the vertical for Rayleigh waves. The dashed and dotted black lines are the array resolution limits. The solid green curves are picked from the data, where the central line indicates the best values and the two outer curves the standard deviation.

5.3 Cross-correlation and Interferometric Multichannel Analysis of Surface Waves (IMASW)

We combine the advantages of active shot data (known source location and high frequency content) and passive microtremor recordings (low frequency content) by using the interferometric principle (Snieder, 2004; Curtis et al., 2006; Schuster, 2009; Wapenaar et al., 2010) to estimate the correlation functions from the vertical components of distinct receiver pairs. The resulting correlograms, assuming the equivalence between the inter-station cross-correlation time derivative pair and the Green's function can be re-ordered according to the respective inter-station distance to build a virtual active experiment setup (Figure 9). We then apply the Interferometric Multichannel Analysis of Surface Waves (IMASW) method to extract the phase velocity dispersion curve of Rayleigh waves (Gouédard et al., 2008; Lontsi et al., 2016). For the IMASW analysis, we only use correlation functions with 100 m maximum inter-station distance (see blue box in Figure 9). For this subset, a clear propagation of Rayleigh waves can be observed. Figure 9 (bottom) shows the IMASW results. The dispersion characteristic of the Rayleigh waves is identified and manually picked in the frequency range between 9 and 16 Hz.

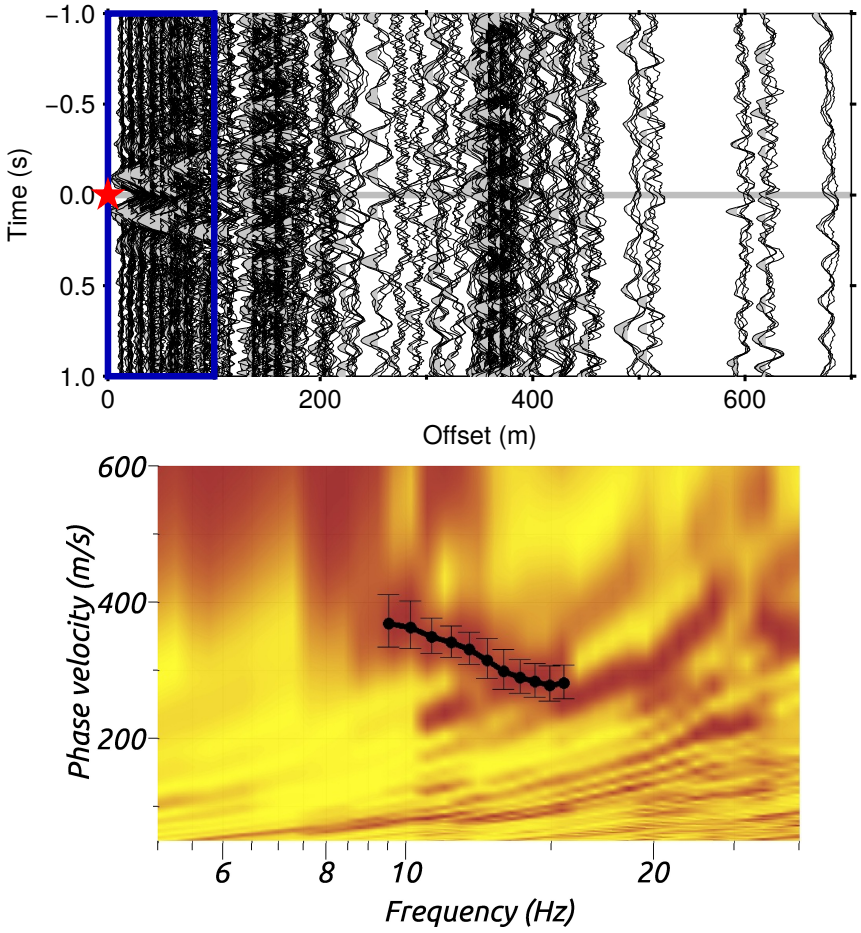

Figure 9: Top: Resulting cross-correlation Green's functions from 120 receiver pair combinations (See array setup in Figure 2). The red star represents the virtual source. The blue box define correlograms with interstation distances less than 100 m. Propagating Rayleigh waves can be observed in this box. Bottom: IMASW results from the cross-correlation functions. A phase velocity dispersion branch is observed and manually picked between 9 and 16 Hz.

5.4 WaveDec

The WaveDec (Maranò et al., 2012) results are shown in Figure 10. Clear phase velocity dispersion curves are observed for both Rayleigh and Love waves in the frequency range from 1.55 to 15.67 Hz. Two branches are picked for the Rayleigh waves, for which it is again not clear to which mode they should be attributed. The ellipticity curve was picked in the frequency range of the Rayleigh wave dispersion curve. We obtained two Rayleigh wave ellipticity angle curves corresponding to the Rayleigh wave dispersion branches. The first Rayleigh wave branch, picked from 1.81 to 3.16 Hz, shows negative ellipticity angles, i.e. retrograde particle motion. The second picked branch shows prograde particle motion from 3.43 to approximately 5.18 Hz and retrograde one from approximately 5.18 to 12.33 Hz. However, the transition at about 5.18 Hz does not seem to belong to the fundamental mode because in that case, there should be a trough visible at this frequency in the H/V curves. Therefore, we conclude that the curves picked from 3.43 to 5.18 Hz and 5.18 to 12.33 Hz belong to two different modes.

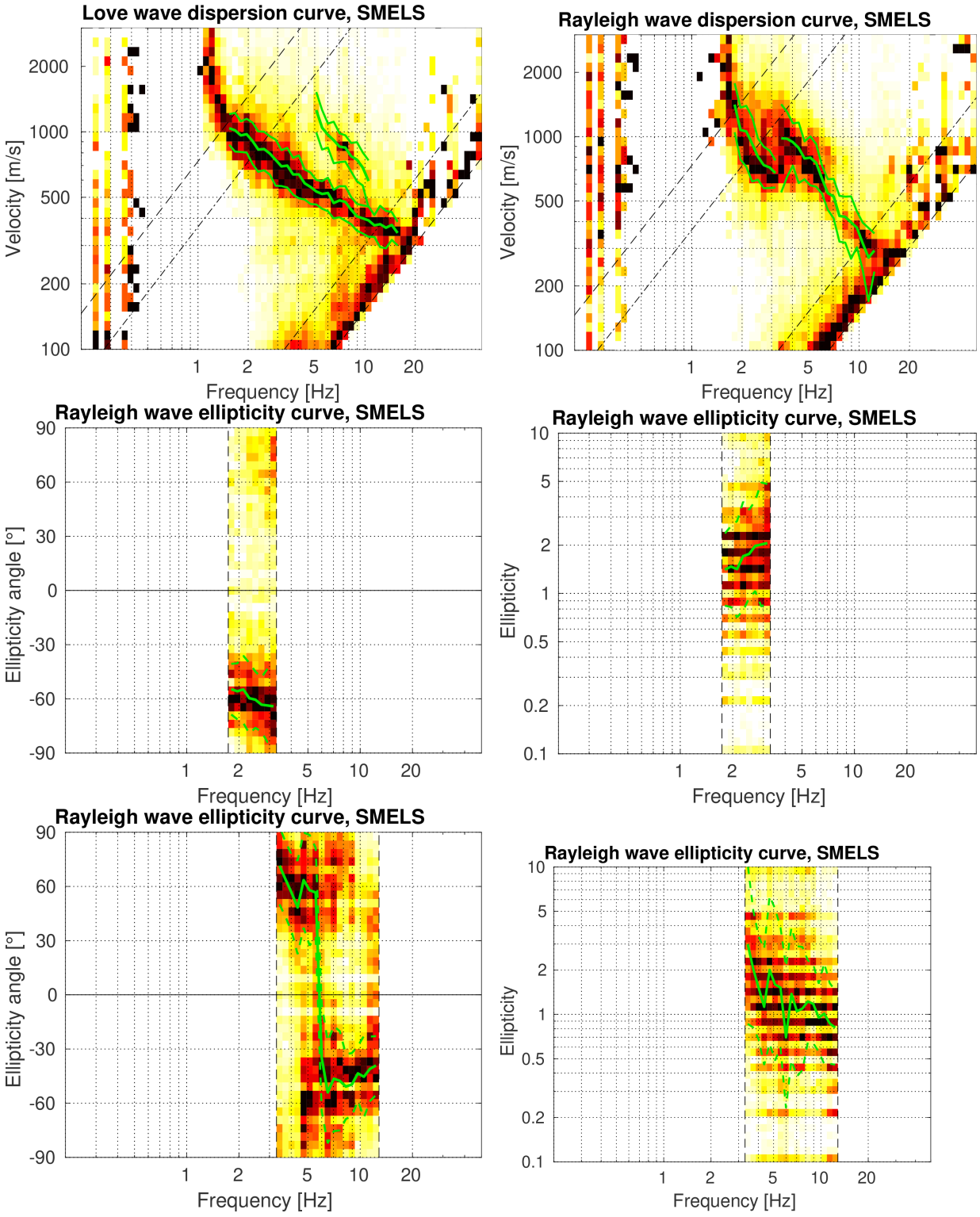

Figure 10: WaveDec results: ellipticity and phase velocity dispersion curves for Rayleigh and Love waves. The phase velocity dispersion branches are picked within the array resolution limits. The solid green curves are picked from the data, where the central line indicates the best values and the two outer curves the standard deviation.

5.5 Overview and discussion of the measurement results

A summary of the estimated dispersion curve branches using the HRFK, WaveDec, IMASW, and SPAC methods is presented in Figure 11.
The Love wave dispersion branches for the high-resolution f-k and WaveDec are in good agreement.
The interpretation of the Rayleigh wave dispersion characteristic is not trivial in the frequency range between 3 and 6 Hz. The reason is that we have two distinct branches below 3 Hz and one branch above 6 Hz. The branch separation is not clear. Above 6 Hz, the Rayleigh wave dispersion curves are in good agreement with each other for all methods. For the next steps, we try to interpret the Rayleigh waves between 2.66 Hz and 16.71 Hz and the Love waves between 1.75 to 10.12 Hz.
Assigning a mode number to the velocity dispersion branches is an important step towards a reliable combined inversion. To interpret the different branches of the velocity dispersion curves, a blind mode search was performed. One branch was assigned the fundamental mode and additional branches were allowed to correspond to any (higher) mode. It comes out that the Rayleigh wave dispersion curve branches correspond to the fundamental and first higher modes (11b and 11c), respectively, and the Love wave branch corresponds to the fundamental mode (see Figure 11e) and first higher mode (see Figure 11f). This interpretation is in line with the WaveDec results for which the curves picked from 3.43 to 5.18 Hz and 5.18 to 12.33 Hz belong to two distinct modes.
The ellipticity curves estimated using RayDec, and WaveDec are shown in Figure 11(g). The RayDec curve for station SMELS55, the central station of the array, shows a fundamental peak at 1.15 Hz. The curves from the other stations of the array are consistent with this fundamental peak (see Figure 4). The WaveDec ellipticity curve is in good agreement with the RayDec curve. The microtremor H/V spectral ratio is also shown in Figure 11(g).
For the combined inversion, the interpreted ellipticity and dispersion curves of Rayleigh and Love waves are used (Figure 11).
A second inversion is performed testing the full microtremor H/V inversion scripts constrained with the dispersion curves to retrieve the shear wave velocity profile.

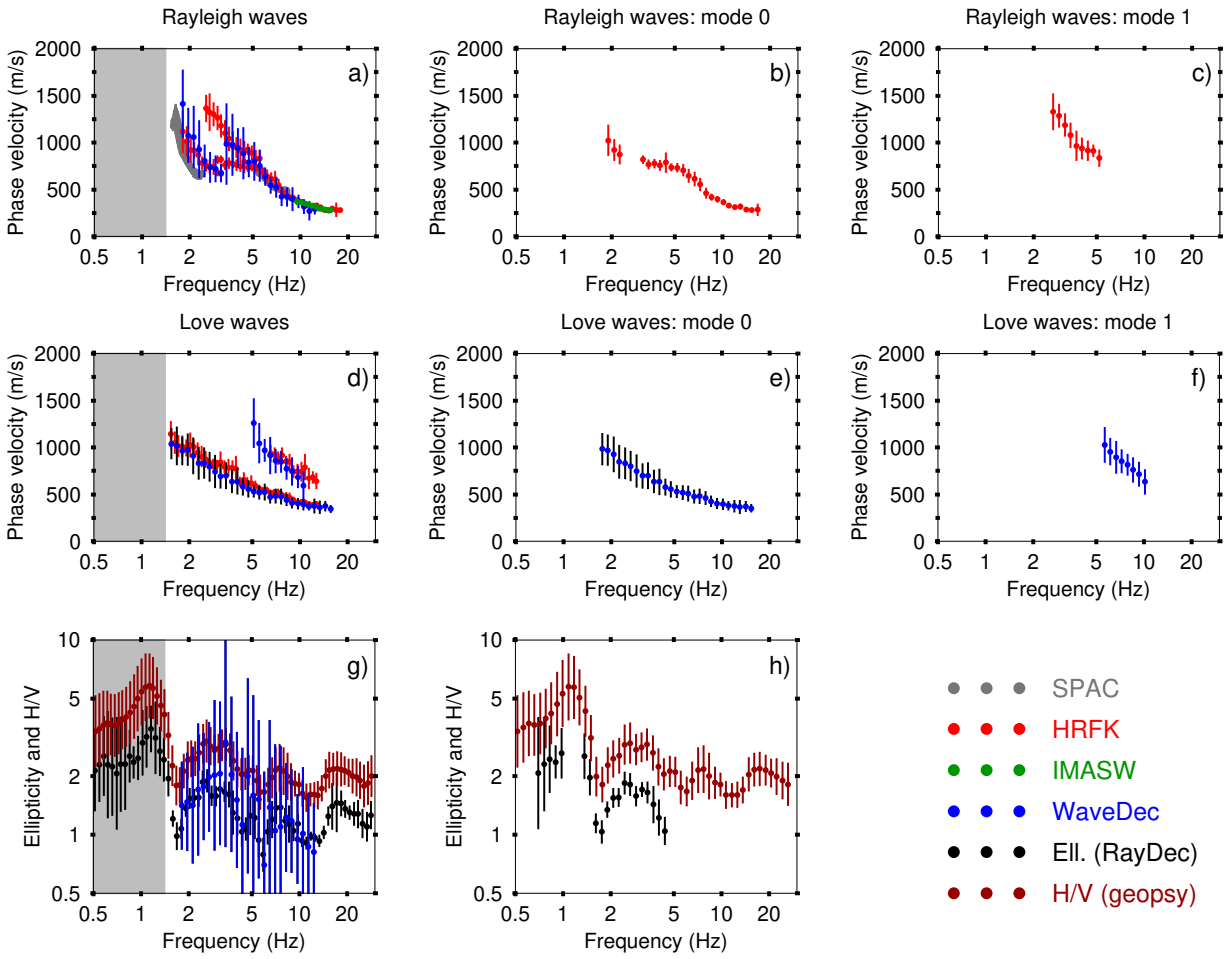

Figure 11: Overview of the results and interpreted curves obtained using the different analysis methods. a) Estimated Rayleigh wave dispersion curves. b) Interpreted Rayleigh wave phase velocity fundamental mode. c) Interpreted Rayleigh wave phase velocity first higher mode. d) Estimated Love wave dispersion curves. e) Interpreted Love wave phase velocity fundamental mode. f) Interpreted Love wave phase velocity first higher mode. g) Estimated microtremor H/V spectral ratio and Rayleigh wave ellipticity. h) Black dots indicate the ellipticity information below 4.4 Hz. Data points around the singularity are excluded. This information is used together with the peak frequency at 1.15 ± 0.1 Hz and the dispersion curve information in the inversion. Red dots indicate the microtremor H/V spectral ratio used to test the full H/V inversion script constrained by the dispersion curve information. The gray box (see a,d,g) indicates additional frequency points from the ellipticity or H/V. This additional information is usesul in the inversion for constraining the bedrock depth.

6 Inversion

6.1 Parametrization

The inversion assumes a layered earth structure. Three, four, five, six and seven layers over half-space were used, as well as a parameter space with FixedLayer depths. The inversion uses the global search neighborhood algorithm (Sambridge, 1999; Wathelet, 2008). The process is started with a set of 50 models. In each iteration step, 50 new models are generated and the 50 best models are kept for further analysis. The process is iterated a large number of times, in this case 4000 times. This results in 200050 generated models. The choice of the parameters for the neighborhood algorithm ensures that we sufficiently explore and exploit the parameter space.
For the full H/V test inversion, one parametrization with seven layers over half-space was used.

6.2 Results

Figures 12-17 show the surface wave inversion results. The full H/V inversion results are shown in Figure 18. We summarize and interpret the best profiles from the inversion in Figure 19. Table 1 gives a summary of the minimum misfit values achieved in each case during the inversion process.

Table 1: Minimum misfit values for different parametrizations.

Parametrization	Minimum misfit
3LOH	0.51
4LOH	0.48
5LOH	0.39
6LOH	0.37
7LOH	0.40
FixedLayer	0.41
7LOH (H/V)	0.35

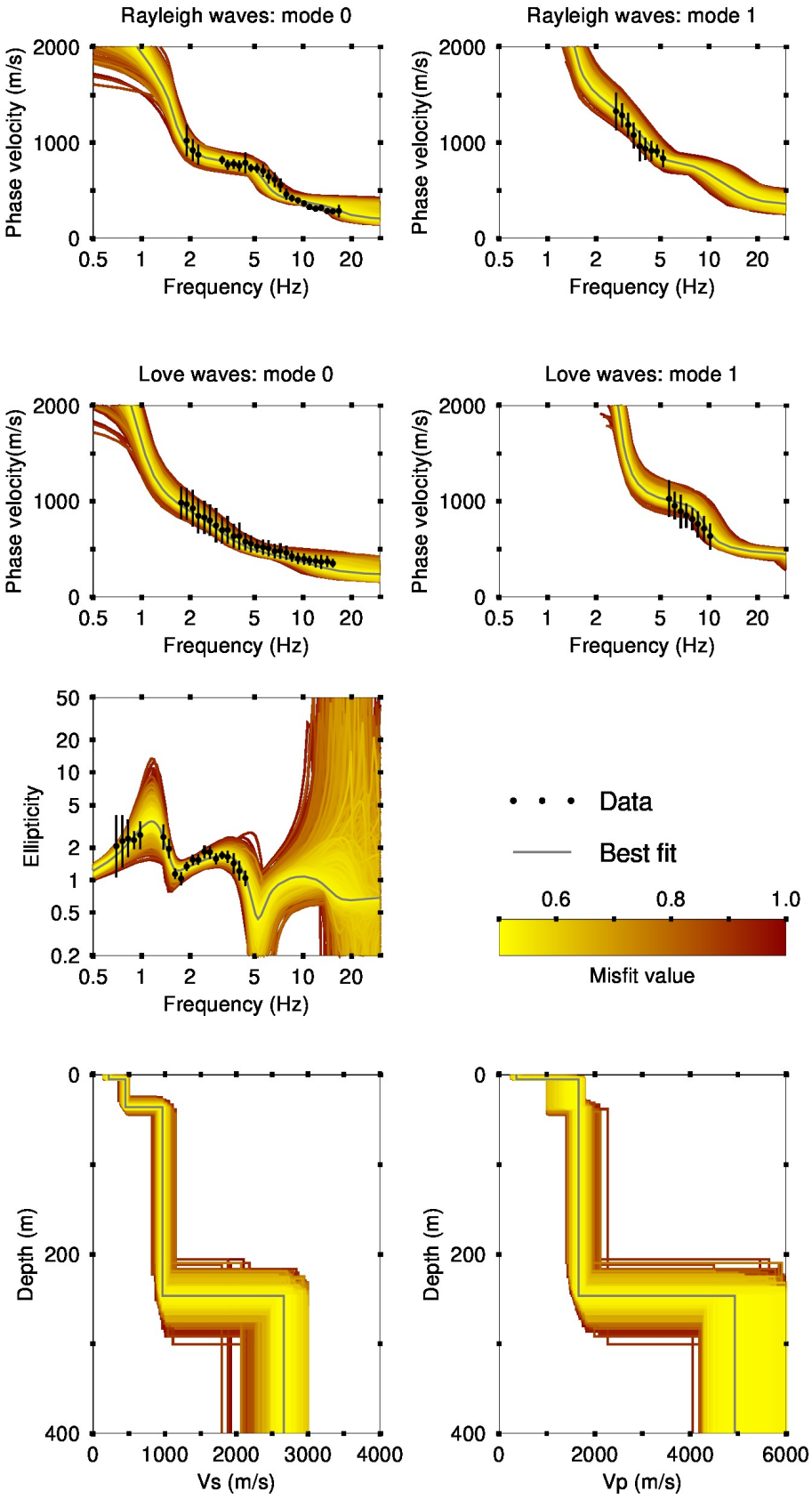

Figure 12: Inversion results using a 3LOH parametrization. The different models are shown in a color according to the misfit value, where the best model is shown in continuous grey color and the black dots indicate the data points that contribute to the inversion. The peak frequency at 1.15 ± 0.1 Hz is used as additional information to further constrain the bedrock depth.

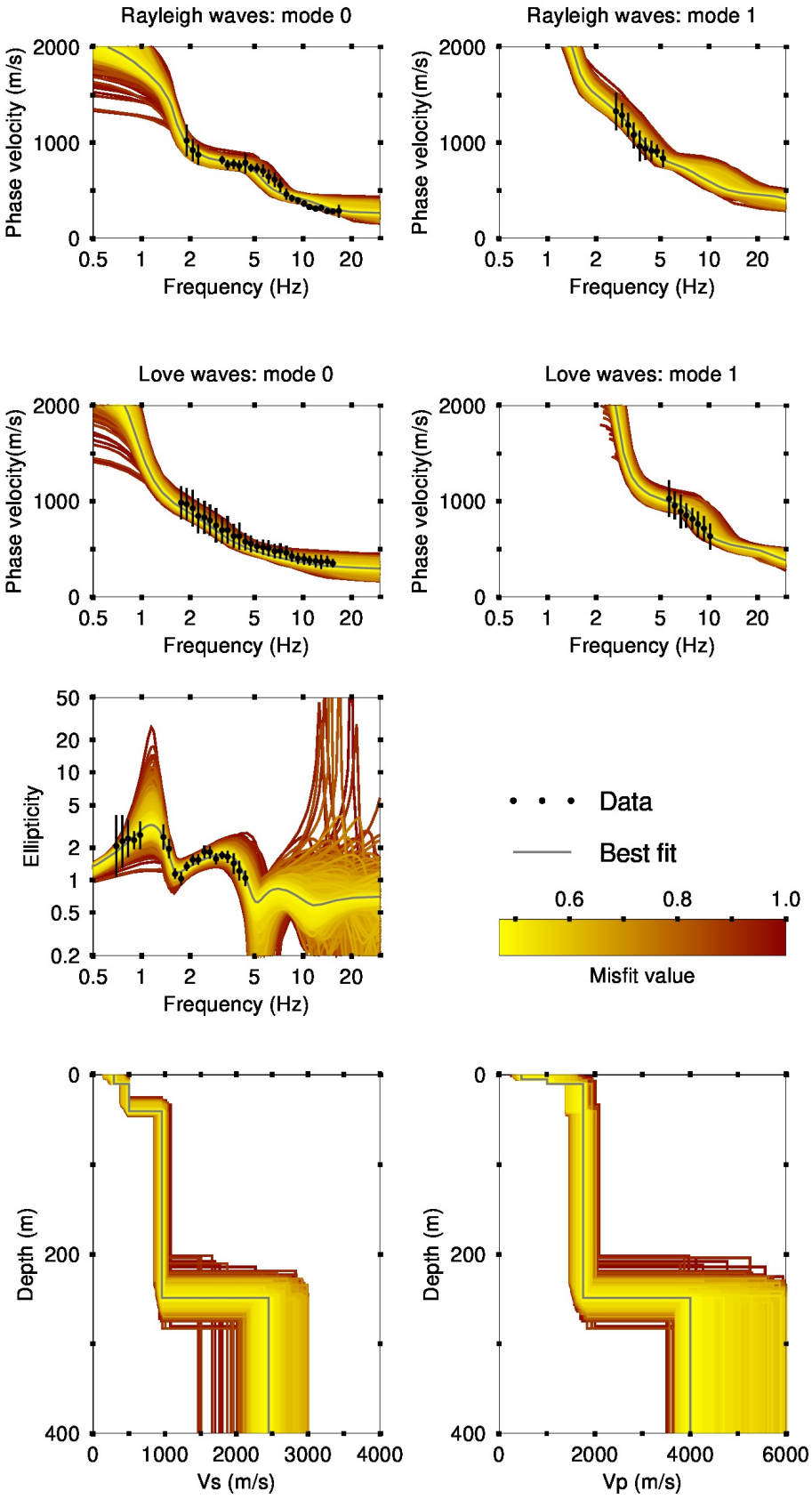

Figure 13: Inversion results using a 4LOH parametrization. The different models are shown in a color according to the misfit value, where the best model is shown in continuous grey color and the black dots indicate the data points that contribute to the inversion. The peak frequency at 1.15 ± 0.1 Hz is used as additional information to further constrain the bedrock depth.

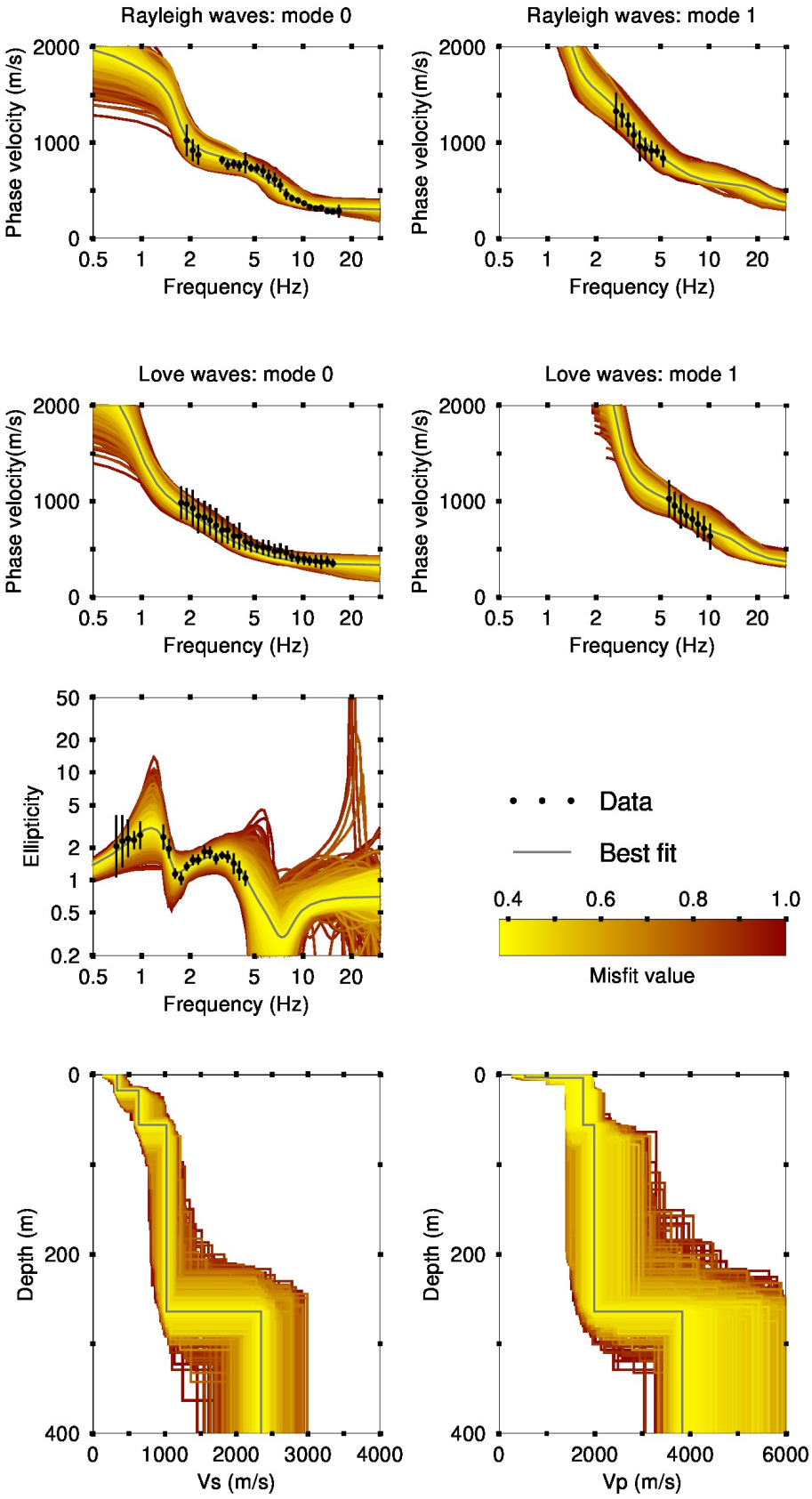

Figure 14: Inversion results using a 5LOH parametrization. The different models are shown in a color according to the misfit value, where the best model is shown in continuous grey color and the black dots indicate the data points that contribute to the inversion. The peak frequency at 1.15 ± 0.1 Hz is used as additional information to further constrain the bedrock depth.

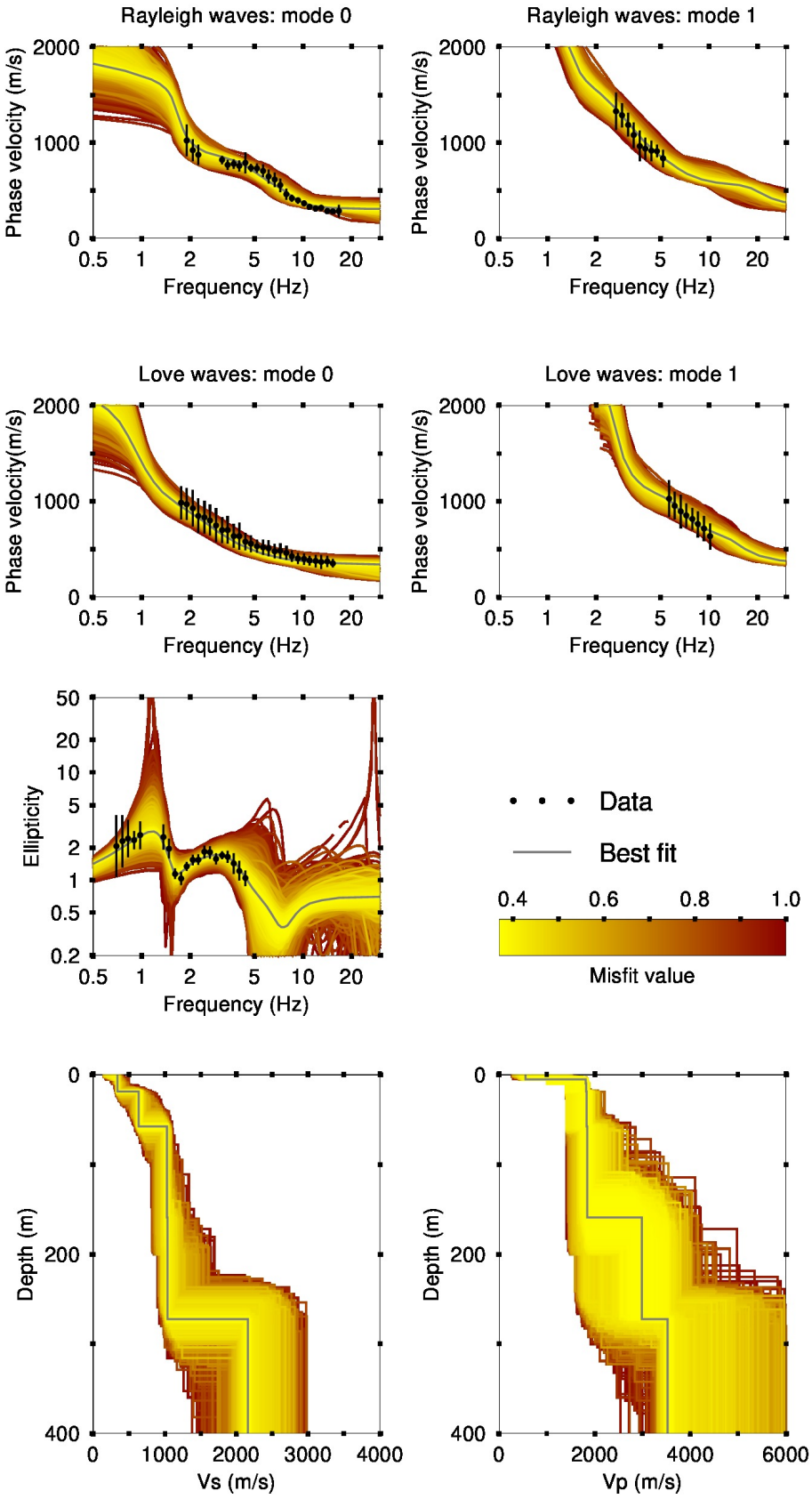

Figure 15: Inversion results using a 6LOH parametrization. The different models are shown in a color according to the misfit value, where the best model is shown in continuous grey color and the black dots indicate the data points that contribute to the inversion. The peak frequency at 1.15 ± 0.1 Hz is used as additional information to further constrain the bedrock depth.

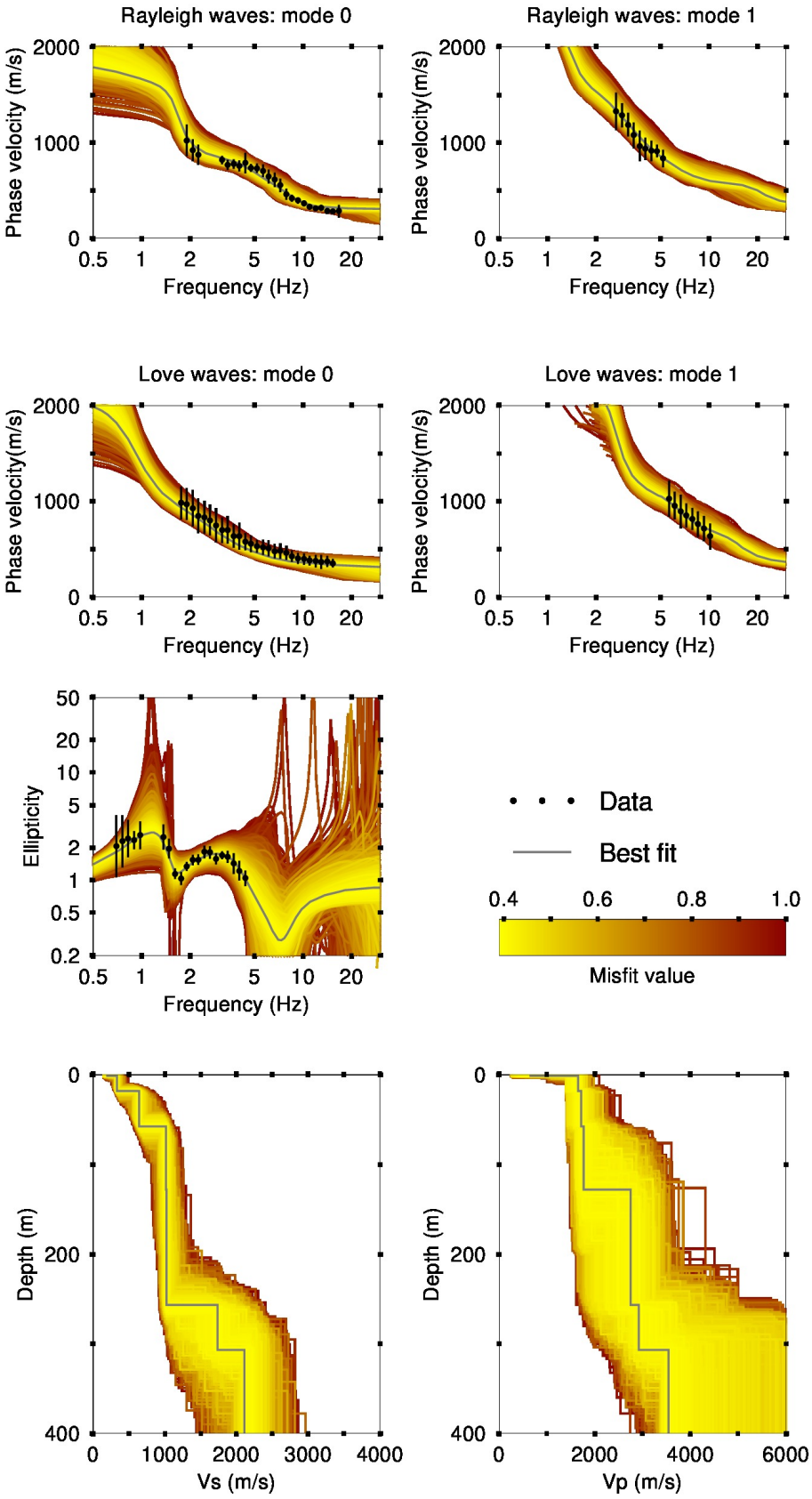

Figure 16: Inversion results using a 7LOH parametrization. The different models are shown in a color according to the misfit value, where the best model is shown in continuous grey color and the black dots indicate the data points that contribute to the inversion. The peak frequency at 1.15 ± 0.1 Hz is used as additional information to further constrain the bedrock depth.

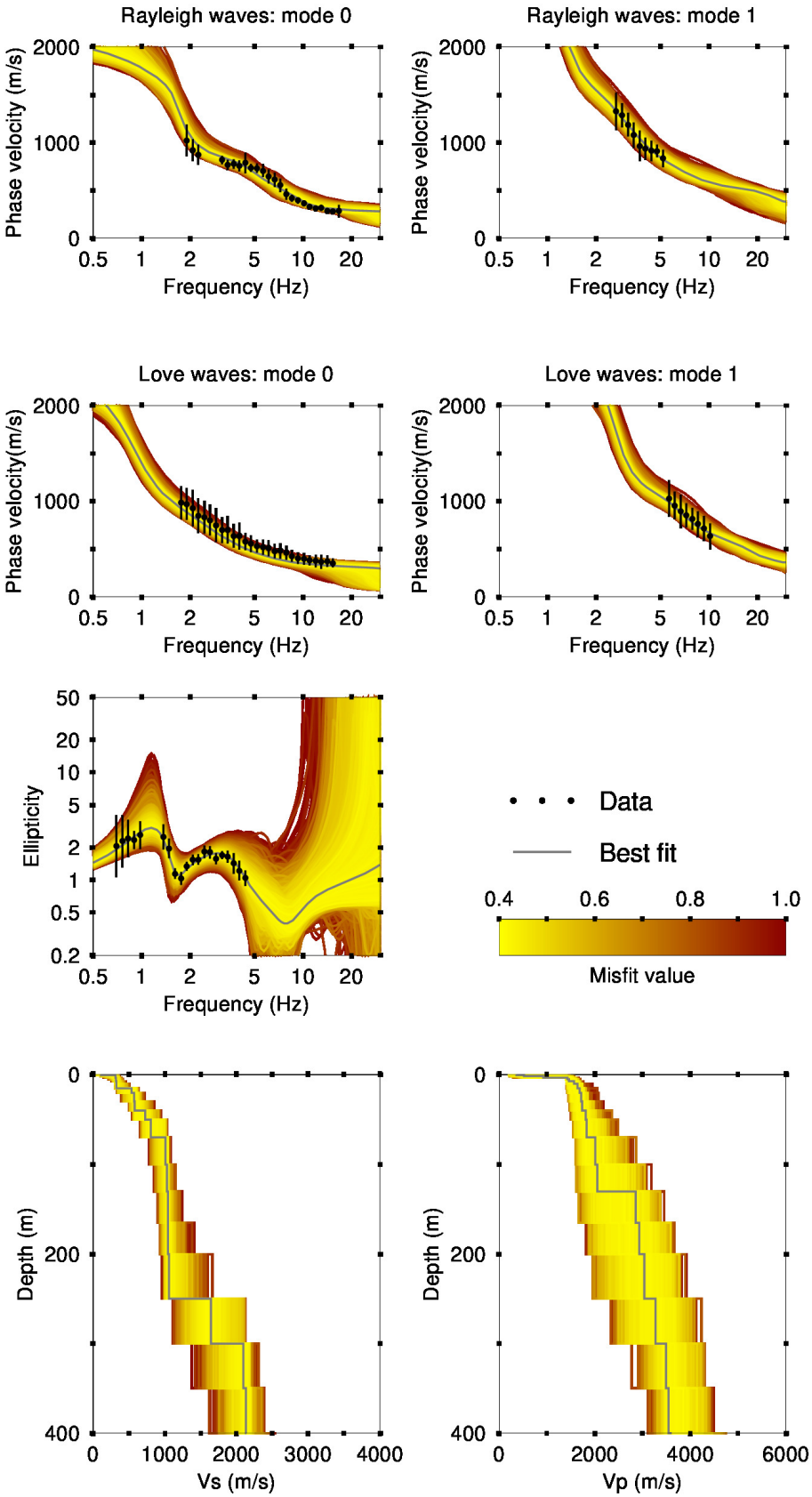

Figure 17: Inversion results using a FixedLayer thickness parametrization. The different models are shown in a color according to the misfit value, where the best model is shown in continuous grey color and the black dots indicate the data points that contribute to the inversion. The peak frequency at 1.15 $\pm$ 0.1 Hz is used as additional information to further constrain the bedrock depth.

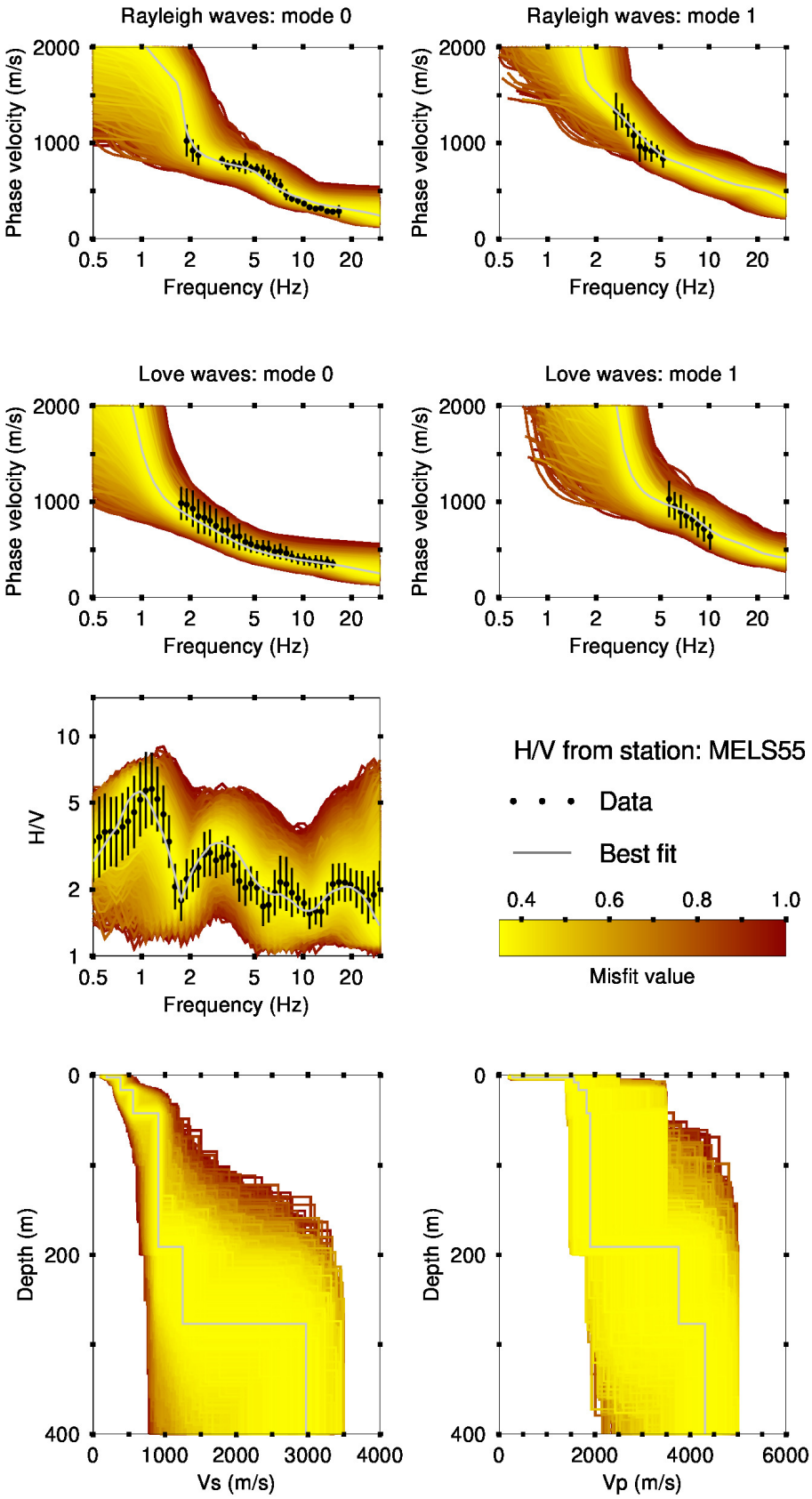

Figure 18: Full microtremor H/V spectral ratio inversion results using a 7LOH parametrization. The different models are shown in a color according to the misfit value, where the best model is shown in continuous grey color and the black dots indicate the data points that contribute to the inversion.

6.3 Inversion summary

The best models from the inversions using different parametrizations (3LOH, 4LOH, 5LOH, 6LOH, 7LOH, and FixedLayer) are shown in Figure 19.

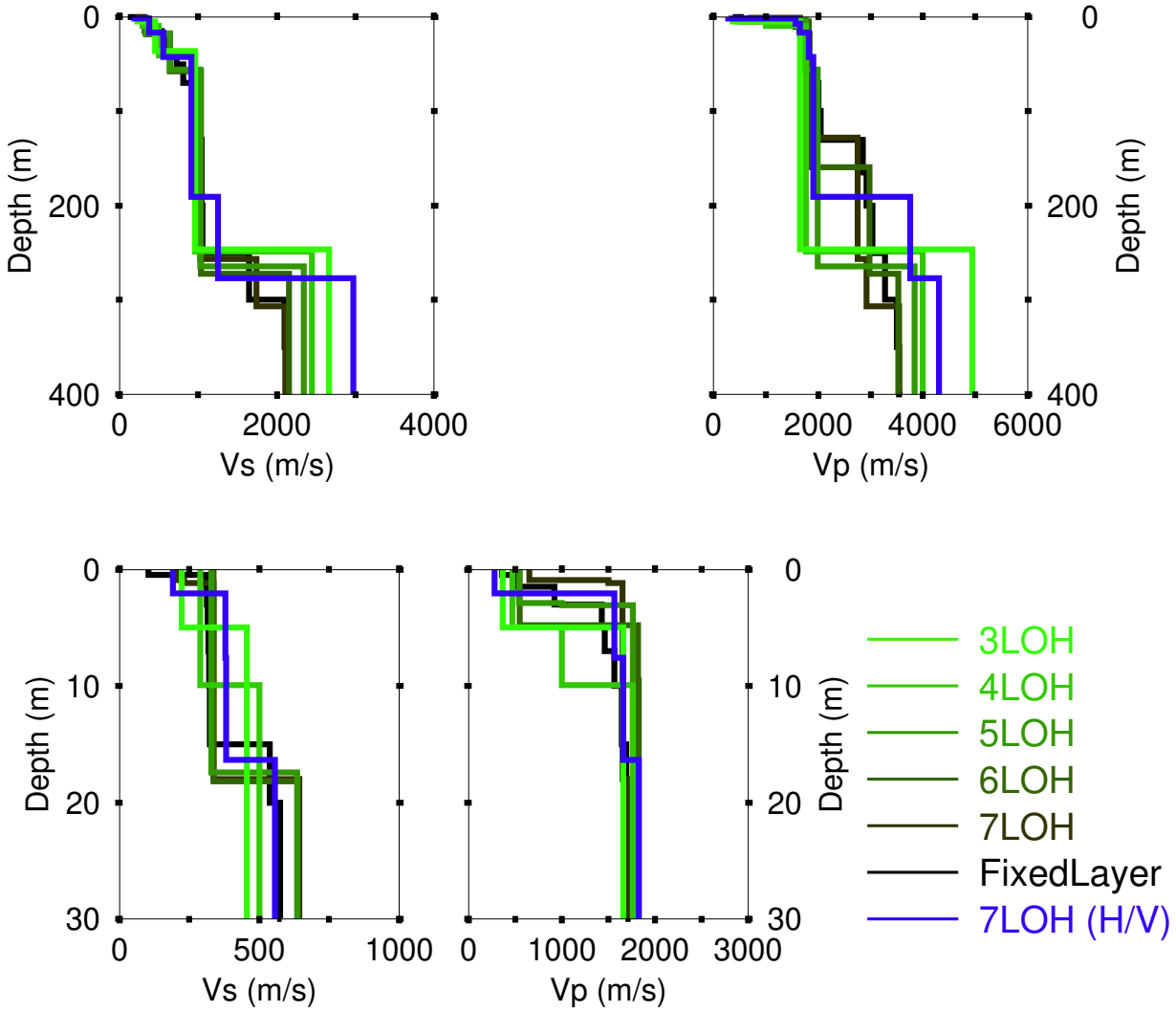

Figure 19: Overview of the best models for the different parameterizations. Top: S-wave (left) and P-wave (right) velocity profiles. Bottom: Zoom on the superficial 30 meters. The velocity profiles represented with the green color are the best models from surface wave inversion and the profile in blue is the best profile from the full H/V spectral ratio inversion with phase velocity dispersion curves as constraint.

The misfit values from the combined inversion vary between 0.35 and 0.50. A much smaller misfit is obtained for model parametrizations with more than 4LOH. A comparison of the velocity profiles indicate that models with more than 4LOH have velocity estimates that are comparable at all depths. We therefore exclude the 3LOH and 4LOH models and keep the other models as representative of the subsurface structure at SMELS. For the 5LOH, 6LOH, 7LOH, and FixedLayer parametrizations, three common discontinuities at about 18, 60 and 260 m are observed. The average V_{S30} from the four best models in the surface wave inversion is 404.4 $\pm$ 9.5 m/s. The V_{S30} is 411.1 m/s in the full H/V inversion. These V_{S30} are comparable and correspond to ground type B in EC8 (European standard) and to ground type C in SIA261 (Swiss standard).

7 Site amplification

Starting from the four best models (5LOH, 6LOH, 7LOH, and FixedLayer) presented in Figure 19, the theoretical site amplification function is computed and compared with the empirical site amplification function of the station SMELS. The site amplification function is estimated following Edwards et al. (2013). The comparison is shown in Figure 20. We also use the best model from full microtremor H/V spectral ratio inversion to compute the theoretical site amplification function. The comparison is also shown in Figure 20.

The comparison indicates that the velocity profiles from the inversion are representative of the subsurface structure under station SMELS. The theoretical amplification finds a broad peak of amplification at around 1 Hz. This is in good agreement with the empirical data. Additional peaks at high frequencies are observed and are also in good agreement with the observation. The overall shapes of the empirical and theoretical amplification functions are similar in peak frequency and amplitude.

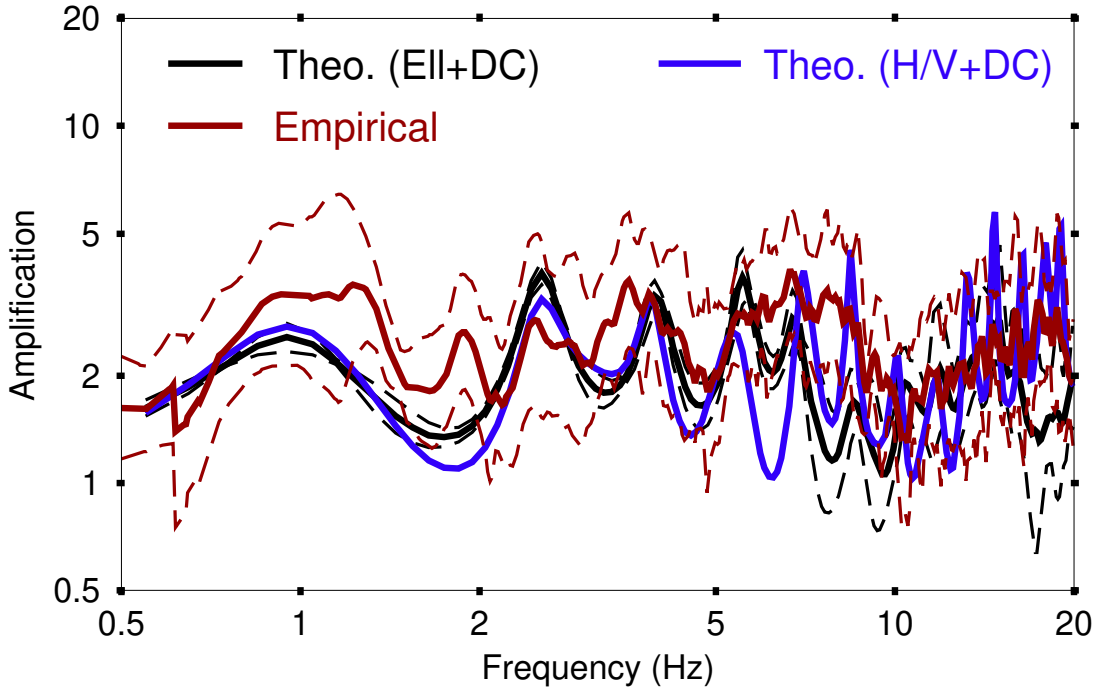

Figure 20: Comparison between the site amplification estimated for the best models from the inversions and the empirical amplification for station SMELS.

8 Quarter-wavelength representation

The quarter wavelength representation for the joint inversion of ellipticity and dispersion curves on one hand and the joint full H/V and dispersion curves on the other hand is presented in Figure 21. The depth resolution is estimated to approximately 350 m using the ellipticity or H/V. Discrepancies in the quarter-wavelength velocity and impedance contrast for the two inversions are prominent for frequencies above 6 Hz.

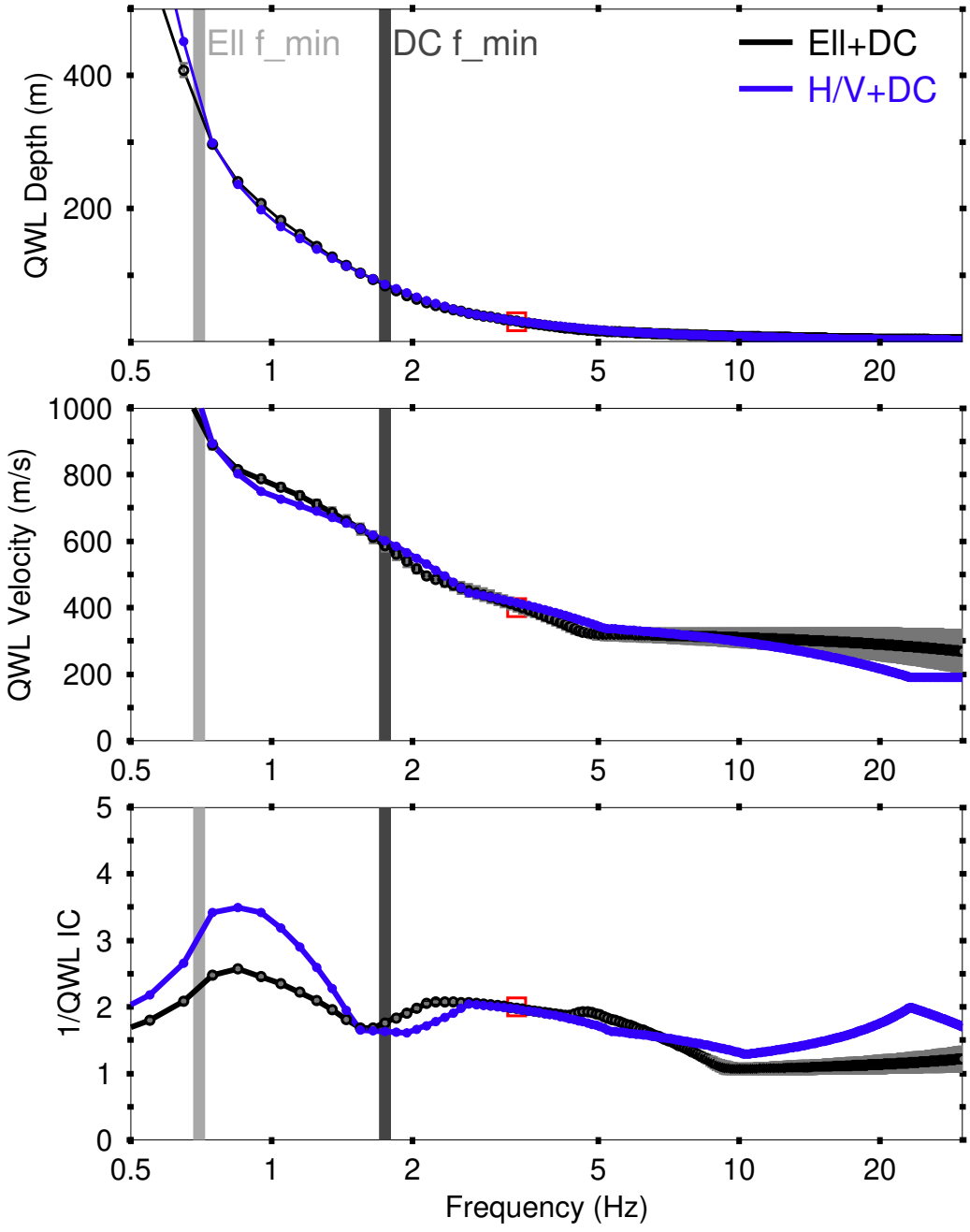

Figure 21: Quarter-wavelength representation for the best models of the inversions. The light and dark grey vertical bars indicate the minimum frequencies for the ellipticity and phase velocities, respectively, used in the inversion process. The solid black line uses the four models from surface wave analysis. The solid blue line is obtained from the interpretation of the full spectrum of the H/V spectral ratio.

9 Conclusion

A passive seismic survey was carried out at the strong motion station SMELS at Mels (SG) to characterize the local subsurface. The dispersion curves for Love and Rayleigh waves were estimated over a wide frequency band ranging from about 1.75 Hz to 16.71 Hz. Two frequency peaks were measured for the ellipticity at around 1.15 and 2.70 Hz. The array methods used were complementary in determining different branches of the dispersion curve. The two inversions allow us to resolve the bedrock depth at about 260 m.
The average V_{S30} is 404.4 $\pm$ 9.5 m/s from the four best models in the surface wave inversion and 411.1 m/s from the best model from full H/V inversion. This V_{S30} value corresponds to ground type B in EC8 (European standard) and to ground type C in SIA261 (Swiss standard).

10 Acknowledgments

The authors thank Stefanie Donner and Monika Bischoff for their help during the array measurements. Vincent Perron assisted in setting up the rotational sensor.

References

Aki, K., 1957. Space and time spectra of stationary stochastic waves, with special reference to microtremors., *Bull. Earthq. Res. Inst.*, **35**, 415–456.

Bettig, B., Bard, P. Y., Scherbaum, F., Riepl, J., Cotton, F., Cornou, C., & Hatzfeld, D., 2001. Analysis of dense array noise measurements using the modified spatial auto-correlation, *Boll. Geof. Teor. Appl.*, **42**, 281–304.

Burjánek, J., Gassner-Stamm, G., Poggi, V., Moore, J. R., & Fäh, D., 2010. Ambient vibration analysis of an unstable mountain slope, *Geophysical Journal International*, **180**(2), 820–828.

Burjánek, J., Moore, J. R., Yugsi Molina, F. X., & Fäh, D., 2012. Instrumental evidence of normal mode rock slope vibration, *Geophysical Journal International*, **188**(2), 559–569.

Curtis, A., Gerstoft, P., Sato, H., Snieder, R., & Wapenaar, K., 2006. Seismic interferometry—turning noise into signal, *The Leading Edge*, **25**(9), 1082–1092.

Edwards, B., Michel, C., Poggi, V., & Fäh, D., 2013. Determination of Site Amplification from Regional Seismicity: Application to the Swiss National Seismic Networks, *Seismological Research Letters*, **84**(4), 611–621.

Fäh, D., Kind, F., & Giardini, D., 2001. A theoretical investigation of average H/V ratios, *Geophysical Journal International*, **145**(2), 535–549.

Fäh, D., Wathelet, M., Kristekova, M., Havenith, H.-B., Endrun, B., V., G. S., Poggi, Burjanek, J., & Cornou, C., 2009. Using ellipticity information for site characterisation using ellipticity information for site characterisation, *Technical report, NERIES JRA4*.

Gouédard, P., Cornou, C., & Roux, P., 2008. Phase–velocity dispersion curves and small-scale geophysics using noise correlation slantstack technique, *Geophysical Journal International*, **172**(3), 971–981.

Hobiger, M., Bard, P.-Y., Cornou, C., & Le Bihan, N., 2009. Single station determination of Rayleigh wave ellipticity by using the random decrement technique (RayDec), *Geophysical Research Letters*, **36**(14), n/a–n/a, L14303.

Lontsi, A., Ohrnberger, M., & Krüger, F., 2016. Shear wave velocity profile estimation by integrated analysis of active and passive seismic data from small aperture arrays, *Journal of Applied Geophysics*, **130**, 37 – 52.

Maranò, S., Reller, C., Loeliger, H.-A., & Fäh, D., 2012. Seismic waves estimation and wavefield decomposition: application to ambient vibrations, *Geophysical Journal International*, **191**(1), 175–188.

Poggi, V. & Fäh, D., 2010. Estimating rayleigh wave particle motion from three-component array analysis of ambient vibrations, *Geophysical Journal International*, **180**(1), 251–267.

Sambridge, M., 1999. Geophysical inversion with a neighbourhood algorithm—i. searching a parameter space, *Geophysical Journal International*, **138**(2), 479–494.

Schuster, G., 2009. Seismic interferometry, *Cambridge University Press*.

Snieder, R., 2004. Extracting the Green's function from the correlation of coda waves: A derivation based on stationary phase, *Phys. Rev. E*, **69**, 046610.

Wapenaar, K., Draganov, D., Snieder, R., Campman, X., & Verdel, A., 2010. Tutorial on seismic interferometry: Part 1 — basic principles and applications, *Geophysics*, **75**(5), 75A195–75A209.

Wathelet, M., 2008. An improved neighborhood algorithm: Parameter conditions and dynamic scaling, *Geophysical Research Letters*, **35**(9).